Deep Learning at the Physical Layer for Adaptive Terahertz Communications

Jacob Hall, *Member, IEEE*, Josep Miquel Jornet, *Senior Member, IEEE*, Ngwe Thawdar, *Member, IEEE*, Tommaso Melodia, *Fellow, IEEE*, and Francesco Restuccia, *Senior Member, IEEE*

***Abstract*—Wireless communications in the terahertz (THz) band will become a cornerstone of sixth-generation (6G) networks. The THz channel, however, presents several challenges, such as distance-dependent absorption coefficients that can change the bandwidth significantly in case of mobility. Thus, future THz transmitters will have to switch modulation and bandwidth almost continuously. Moreover, using the same transmission scheme can enable adversaries to leverage smart interfering to inflict more damage with less energy expense. To help enable adaptive and secure THz communications, this article presents the first ever experimental study of modulation and bandwidth classification (MBC) at THz frequencies through deep learning (DL) techniques. We have performed an extensive experimental data collection campaign at 120 GHz with different modulation schemes, signal bandwidth (up to 20 GHz), and different signal-to-noise ratio (SNR) levels. We prove for the first time the feasibility and effectiveness of MBC at THz frequencies, with our DL models reaching accuracy up to 78% and 90% in low- and high-SNR conditions. Furthermore, we investigate the memory and latency constraints that need to be satisfied as a function of the signal bandwidth, and propose a boosting technique to improve the inference quality by trading off latency for accuracy. Finally, we experimentally evaluate the latency of our CNN models through FPGA implementation.**

***Index Terms*—Deep learning (DL), experiments, modulation and bandwidth classification (MBC), sixth generation (6G) terahertz (THz) communications, wireless.**

I. Introduction

RADIO frequency (RF) spectrum has become one of the most scarce resources available nowadays. Ericsson's latest report forecasts that fifth-generation mobile subscriptions will reach 3.5 billion in 2026, with worldwide data traffic surpassing 200 exabytes per month [1]. These numbers clearly show that in a few years, existing spectrum bands below 6 GHz (sub-6-GHz) will become saturated. Thus, a significantly large number of wireless devices will need to migrate to less congested spectrum bands. Given the lack of continuous large chunks of bandwidth (BW) in other frequency bands [2], the upper millimeter wave (mmWave) and terahertz (THz) bands [3]—located between 0.1 and 10 THz of the RF spectrum—will be used to relieve the current spectrum crunch at lower frequencies. Ultimately, this is because ultra-high-BW wireless links able to multiplex thousands of users at the same time are possible at THz frequencies [4]. Beyond addressing spectrum congestion, the THz band will unleash a digital transformation in our society, by enabling game-changing applications such as real-time virtual reality/augmented reality, holographic telepresence, and Industry 4.0 [5], [6].

Although the THz channel presents unique opportunities, it also presents a series of unique challenges that are absent in traditional wireless propagation environments. Indeed, the path loss in the THz band is strongly impacted by the molecular absorption loss, which depends on *time- and distance-dependent factors* such as the concentration and the particular mixture of molecules encountered (particularly water vapor) along the path, as observed in [7]. Thus, THz channels are extremely frequency-selective, with BW severely shrinking or expanding over time as a function of the distance between the transmitter (TXer) and the receiver (RXer) or the ambient humidity, which also requires significant adaptability in terms of physical layer (PHY) waveforms used for transmission.

Indeed, THz frequencies are naturally more secure due to their unique distance-dependent BW and high directivity. However, it has been shown that they are still susceptible to interference and eavesdropping [8], [9], [10], [11], [12]. While such work focuses on security from a propagation standpoint, we also point out that flexibility in PHY parameters can provide additional security to wireless signals. It is well studied in the literature that fixed parameters of wireless transmission schemes can make the systems vulnerable to interference and hence affect overall system throughput. For example, Vo-Huu et al. [13] have shown that deterministic and predictable structure of the interleavers and coded bits in the 802.11 a/g/n coding scheme can reveal a subcarrier-level pattern, which is not a desirable effect for system security. Clancy [14] has also pointed out the vulnerability of orthogonal frequency division multiplexing (OFDM) scheme that are common in cellular and wireless local area networks, due to its repeated use of pilot tones. Therefore, it is paramount from the system security point of view that future wireless systems should employ extremely flexible PHY, and TXer and

Manuscript received 28 February 2022; revised 16 October 2022 and 16 December 2022; accepted 3 January 2023. Date of publication 19 January 2023; date of current version 3 March 2023. This work was supported in part by the US Air Force Research Laboratory under Grant FA8750-20-1-0200 and in part by the US National Science Foundation under Grant CNS-2011411. *(Corresponding author: Jacob Hall.)*

Jacob Hall and Ngwe Thawdar are with Air Force Research Laboratory Information Directorate, Rome, NY 13441 USA (e-mail: jacob.hall.49@us.af.mil; ngwe.thawdar@us.af.mil).

Josep Miquel Jornet, Tommaso Melodia, and Francesco Restuccia are with the Institute for the Wireless Internet of Things, Northeastern University, Boston, MA 02115 USA (e-mail: jmjornet@northeastern.edu; t.melodia@northeastern.edu; f.restuccia@northeastern.edu).

Color versions of one or more figures in this article are available at https://doi.org/10.1109/TTHZ.2023.3237697.

Digital Object Identifier 10.1109/TTHZ.2023.3237697

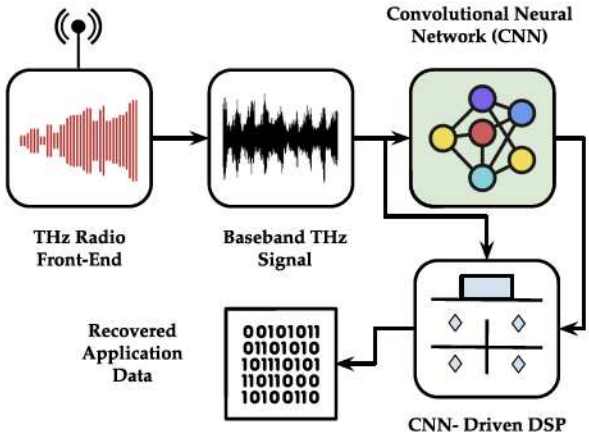

Fig. 1. MBC in THz networks through DL at the PHY.

RXer designs to support the new flexible signaling schemes. By continuously and seamlessly changing the PHY parameters, it follows that the transmission scheme becomes not only more effective, but also more resilient from a security standpoint.

The aforementioned reasons call for extremely flexible and adaptive PHY protocols where TXer and RXer can change their BW and modulation (MD) without coordination. While the TXer can choose MD and BW through channel state information reports sent periodically by the RXer, to decode the data, the RXer needs to reconfigure the BW of its baseband finite impulse response filter *before the waveform is demodulated*. We define this process as modulation and bandwidth classification (MBC), which is shown in Fig. 1. The received THz signal with variable BW and MD is processed by a THz RF front-end and down-converted from RF to the baseband frequency. The baseband signal is then sent to a convolutional neural network (CNN), which infers BW and MD of the incoming THz signal. The CNN inference would then be used by a reconfigurable digital signal processing (DSP) logic, which proceeds to demodulate and recover the application data.

Although MD classification has been explored in the sub-6-GHz context [15], [16], [17], [18], [19], to the best of our knowledge, BW classification has not been attempted yet. However, this is definitely going to change for THz networks. Although the Institute of Electrical and Electronics Engineers (IEEE) 802.15-3d standard—the only redacted for THz frequencies [20] so far—defines eight different possible BWs that can be used, it does not specify if, when, and how a TXer shall switch to a different BW. For this reason, an investigation into the feasibility of MBC at THz *will directly impact ongoing standardization efforts in the THz band* by the IEEE 802.15 WPAN Terahertz Interest Group, which seeks to explore the usage of THz spectrum for future IEEE standards [21].

What makes the problem of MBC at THz frequency challenging is the extremely high BW of the transmission, which introduces challenges from both a computational and classification standpoint. To the best of our knowledge, the problem of joint MBC in the THz band has not been investigated yet, mostly due to the lack of a well-constructed dataset capturing extremely high-BW transmissions.

In short, the article provides the following key advances.

1) We present the first experimental evaluation of data-driven MBC at THz frequencies. We utilize a custom-tailored experimental testbed to create a large-scale dataset composed by in phase/quadrature (I/Q) samples collected at the 120-GHz RF frequency, with
   a) five MD schemes (BPSK, QPSK, 8PSK, 16QAM, and 64QAM);
   b) three BWs (5, 10, and 20 GHz); and
   c) two signal-to-noise ratio (SNR) levels (low, high), totaling 150 000 frames.

   We propose a system model and evaluate the constraints on memory and latency that the system must satisfy according to the given maximum system BW.
2) We extensively train and test CNN classifiers based on the experimental data collected through our testbed. We first run an extensive hyperparameter exploration by varying the number of convolutional layers (CVLs) and the number of filters of the CNN. Our results show that our CNN classifiers achieve up to 78% and 90% accuracy in the case of low and high SNR, respectively. Next, we propose a novel boosting technique where majority voting among different CNN executions with subsequent frames is used to trade off better accuracy for increased latency. We show that our technique further boosts accuracy by up to 91% and >99% in the low- and high-SNR regimes. We also train with both SNRs to achieve an accuracy of 81% and 92% for standard and boosted testing, respectively. We further investigate the latency/accuracy tradeoff by reporting CNN latency results obtained through FPGA implementation.
3) We provide to the research community wide access to the experimental dataset used in this article, which will act as performance benchmark for every other subsequent work for data-driven classification at THz frequencies. Without this dataset, any subsequent work in this field will necessarily rely on simulation data, which cannot capture the real-world effects imposed by not only the THz channel, but also the frequency selective nature of ultra-broadband THz transceivers and antennas. Our contribution will help addressing the current dearth of datasets in the wireless community. To the best of our knowledge, this is the first work in literature shedding light on this crucial problem, which will inform current standardization efforts in the THz band.

II. Background and Related Work

We first motivate the need of MBC at THz frequencies in Section II-A, then discuss existing work in ML for wireless in Section II-B, and THz security in Section II-C.

A. Problem Motivation

It is well known that the THz propagation environment is significantly challenging and substantially different from the sub-6-GHz and mmWave ones [3], [6], [22]. This is mainly due to the presence of distance-dependent absorption given by

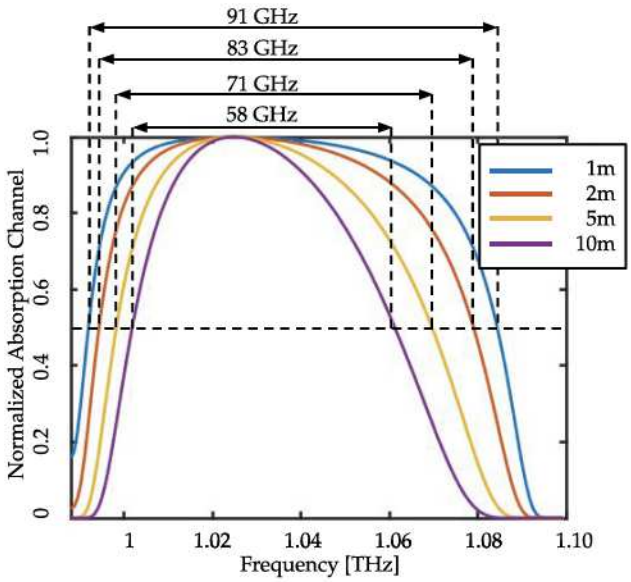

Fig. 2. 3-dB BW in between two absorption lines around 1 THz caused by molecular absorption with water vapor.

water vapor molecules between the TXer and the RXer, which are inevitably present in the atmosphere as long as the ambient humidity is not absolute zero. The photon energy of THz signals induces internal vibrations in molecules, which convert the wave electromagnetic energy into kinetic energy [7]. The situation becomes more challenging in the presence of rain, where in addition to absorption, scattering by water droplets comparable in size to the signal wavelength is present [23].

As humidity levels and TXer–RXer distance are hardly predictable in advance, the resulting THz channel BW is expected to change drastically and dynamically in real-world THz deployments. To further quantify such effect, Fig. 2 shows the normalized channel response around 1.025 THz as a function of frequency caused by molecular absorption with water vapor. While absorption is present throughout the THz band, this provides a clear demonstration of the distance-dependent BW caused by absorption.

These curves were obtained from the model published in [7], and are based on the HITRAN molecular spectroscopic database [24] and radiative transfer theory [25]. We also report the 3-dB BW for each curve. We can observe that the BW increases from 58 to 91 GHz in the span of only 10 m, which is an increase of 56% with respect to the original value. As a consequence, transmission schemes at the THz frequency must be BW- and MD-adaptive to deal with the shrinking and expansion of the channel during the duration of the wireless link, which ultimately motivates our investigation into MBC at THz frequencies.

As yet, a few tailored MDs for THz communications that can dynamically accommodate different BWs have been proposed. In [26], an optimization framework was developed to select the duration and number of THz pulses [27] to be transmitted, as well as the number of molecular-absorption-defined windows to be utilized according to the distance-dependent available BW at THz frequencies. In [28], THz modulators with different MD order and symbol duration were concatenated to generate multiresolution data able to accommodate users at different distances with different SNR and different available BW because of the molecular absorption.

Due to current THz hardware limitations, we are unable to communicate with BWs and distances to experimentally measure a changing absorption window. Thus, our methodology uses our highest capabilities of transmitting with 20 GHz of BW, which we purposefully lower to 10 and 5 GHz to emulate a narrowing absorption window.

B. Related Work in ML for Wireless

Bleeding-edge advances in machine learning (ML) are increasingly being used for dynamic spectrum access [29], [30], [31], [32], optimal multimedia streaming [33], [34], [35], cellular network management [36], [37], rate selection [38], and resource allocation [39], [40], [41], [42], [43]. For an exhaustive survey on the topic, we refer the reader to the excellent survey [44]. PHY classification issues, such as MD recognition, have gained significant momentum over the last few years. However, traditional ML techniques based on feature extraction are computationally expensive, problem specific, and require the manual establishment of decision bounds [15], [16], [17], [18], [19]. Conversely, deep learning (DL) techniques have received significant attention, thanks to the lack of the feature extraction process [45], [46], [47], [48], [49]. Moreover, DL has been demonstrated to be effective for real-time hardware-based implementations, since fine-tuning of the model weights—changeable through software—allows for fast adaptation to adverse channel conditions [50], [51]. In [52], Like et al. provided comparisons between ML models' effectiveness for signal recognition when introduced to multipath fading, while Zhang et al. [53] and Pavlov et al. [54] demonstrated the effectiveness of modern DL approaches to the tougher task of fading channels. Amani et al. [55] further explored multipath in the case of radio fingerprinting.

Among the related work in frequencies below 6 GHz, O'Shea et al. [56] presented several DL models to address MD classification, while Karra et al. [57] identified MD class and order using hierarchical deep neural networks (DNNs). Kulin et al. [58] presented a conceptual framework for end-to-end wireless DL, including a methodology to collect, represent, and classify waveforms using DNNs. At mmWave and THz frequencies (above 30 GHz), DL techniques have been used to classify beam angle and angle of arrival [59], [60], blockage prediction [61], [62], indoor localization [63], [64], and channel estimation [65]. However, most of existing datasets at those frequencies are generated through simulations, which are not able to capture real-world channel effects.

C. Related Work in THz Security

The higher free-space path loss at THz frequencies, combined with molecular absorption, will govern the use of highly directional antennas to complete even short-range links. With

these narrow beamwidths and a frequency selective, distance-dependent channel, it was once assumed that THz communications had improved security in both interference and eavesdropping [66]. However, in recent years, many works have shown otherwise.

Ma et al. [12], demonstrated the ability to eavesdrop a THz signal through the introduction of a scatterer into the narrow transmission beam to deflect the beam in the direction of an eavesdropper. Moreover, the scatterer is transparent to the RXer requiring the TXer to listen for back-scatter in order to detect its presence.

Similarly, highly directional antennas also have side-lobes that can be leveraged to eavesdrop on non-line-of-sight (NLOS) paths. Venkatesh et al. [11] mitigated an eavesdropper's ability by forcing side-lobe emissions to be time varying and spectrally aliased while keeping the main-lobe unaffected. Moreover, Cohen et al. [8] proposed absolute security where the frequency- and location-dependent antenna minima are encoded such that an NLOS eavesdropper cannot see enough signal to decode the transmission. The number of antenna minima increases with wider BWs and greater directivity, making this solution well suited for THz communications.

While the aforementioned work improves PHY layer security from a propagation standpoint, there is also vulnerability to interference in the design of a transmitted packet. Vo-Huu et al. [13] demonstrated that reliance on certain OFDM subcarriers in the 802.11 a/g/n coding scheme allows for highly efficient narrowband interference. Moreover, Clancy [14] showed that the use of predictably placed pilot tones in any OFDM waveform can be leveraged through smart nulling at reduced cost to the interferer. Thus, inflexibility and predictably of frame structures leaves communications systems vulnerable at the PHY layer. While signal classification in literature is primarily tasked to detect other's signals (for example, in cognitive radio), it can be used to secure communications at the PHY layer. By reducing the amount of control information that is transmitted and instead relying upon an adaptive RXer to identify key information from the waveform itself, the more flexible and less predictable PHY layer becomes harder for adversaries to understand or disrupt.

III. Experimental Testbed, Data Collection Procedures, and ML Models

Fig. 3 shows TeraNova [67], the experimental testbed used for our data collection campaign, as well as the positioning of TXer and RXer in our laboratory setting. Our setup leverages radio front-ends manufactured by Virginia Diodes Inc. (VDI), which were custom-designed for the 120–140 GHz frequency range. The 120-GHz TXer has its local oscillator (LO) driven by an analog signal generator (SG), a Keysight PSG E8257D, and employs two frequency doublers (total multiplication of 4x) to bring the PSG signal into the THz range. The transmitted waveform is designed in MATLAB and produced by a Keysight M8196A arbitrary waveform generator (AWG). This intermediate frequency (IF) output is fed into the 120-GHz VDI TXer, where it is mixed with the multiplied LO.

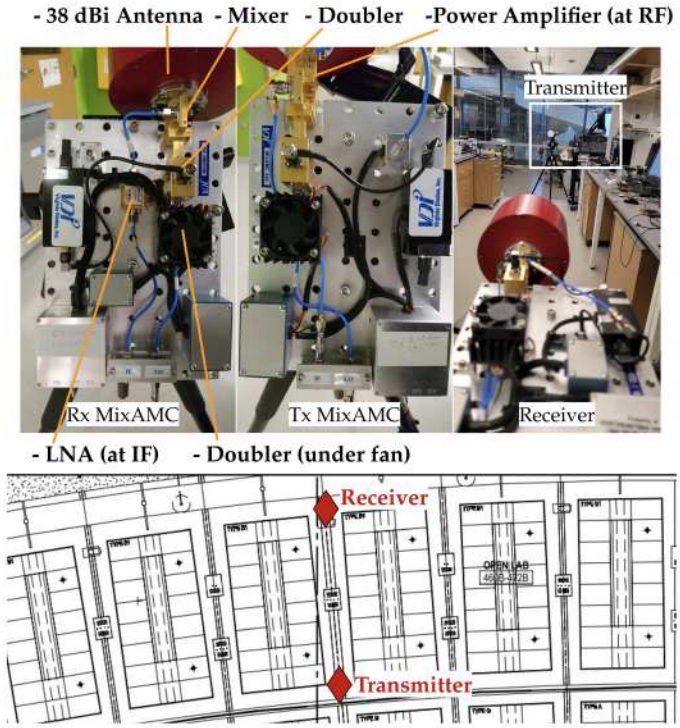

Fig. 3. Experimental testbed, TeraNova, used for data collection and floor layout of the lab environment. The scale of the floor layout is approximately 1 cm:1 m.

The RXer's LO is driven by a separate identical SG, and its downconverted output is read by a Keysight DSOZ632A digital storage oscilloscope (DSO), where the signal can be analyzed and saved. For this experiment, the 120-GHz TXer and RXer were fixed with 38 dBi antennas. The use of the AWG and DSO allowed us to store the received waveforms for further offline processing.

The process for changing transmission BW was accomplished with the flexibility afforded by our communication chain utilizing an AWG, DSO, and MATLAB. The AWG can generate signals with a BW up to 32 GHz; thus, any waveform we design in MATLAB within that range can be transmitted at will. Additionally, the DSO can capture any signal with a BW up to 63 GHz. In our experiments, however, we limit the transmission BW to 20 GHz due to the BW of the radio front-ends. We programmatically control the AWG and DSO with MATLAB to automate changing waveforms and capturing data.

The TXer and RXer were deployed in a laboratory environment in the bottom side of Fig. 3, with a distance of 5 m separating the two link endpoints. The transmissions were dual-side band, and as such the BW of the signal was two times the symbol rate. This gave us a maximum data rate of 60 Gb/s for 64QAM, 20 GHz BW.

A. Data Collection and Dataset Structure

The waveforms produced by the AWG were all centered around the same IF of 20 GHz. The RXer and TXer LO frequency was set to 135 and 125 GHz, respectively, for all transmissions.

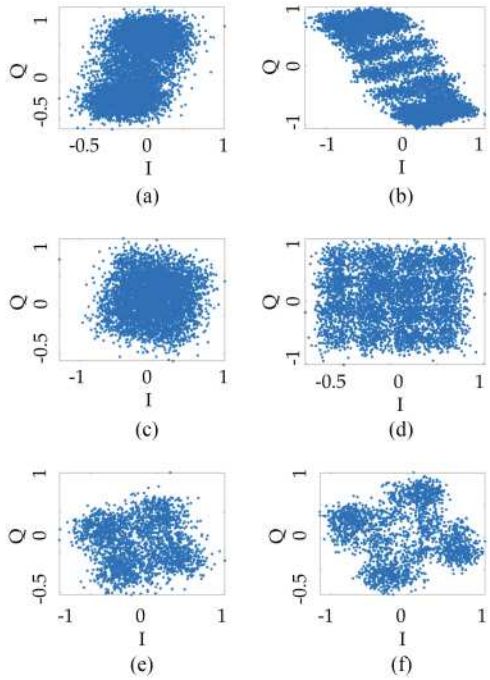

Fig. 4. Recovered I/Q constellations with normalized power. (a) and (b) 5-GHz 2PSK, low and high SNR. (c) and (d) 10-GHz 16QAM, low and high SNR. (e) and (f) 20-GHz 4PSK, low and high SNR.

TABLE I
AVERAGE E_b/N_0 VALUES IN DB FOR ALL SUBSETS OF DATA

BW	E_b/N_0				
SNR Low	2PSK	4PSK	8PSK	16QAM	64QAM
5 GHz	10.10	6.80	5.24	2.65	0.07
10 GHz	8.26	5.57	3.05	0.51	-1.68
20 GHz	5.99	3.65	1.83	-0.17	-3.65
SNR High					
5 GHz	23.21	19.94	18.78	15.57	13.27
10 GHz	22.93	20.54	17.59	15.75	13.07
20 GHz	20.84	18.20	16.48	15.14	12.27

Different LO frequencies are utilized to minimize the impact of the image frequencies and the lack of RF filters at THz-band frequencies. All received waveforms were then centered at an IF of 10 GHz. The PSGs were set to 10 dBm output power. For the two SNR levels recorded, the AWG was set to 75 and 600 mV, for low and high, respectively. Fig. 4 shows I/Q constellations of six different received signals to demonstrate the channel distortion of this setup.

The average E_b/N_0 for each subset was calculated and is displayed in Table I. The lower SNR level caused the QAM MDs to have negative E_b/N_0 for all three BWs (i.e., noise is more powerful than the signal), which represents a very challenging scenario for our classifiers.

In our transmitted packet, we use an 18-bit maximal merit factor sequence [68] for our preamble to perform frame synchronization, which is followed by the data payload. We capture signals using the DSO's fastest sampling rate, 160 giga-samples-per-second (GSa/s), to improve our ability to find the signal in the low-SNR scenario.

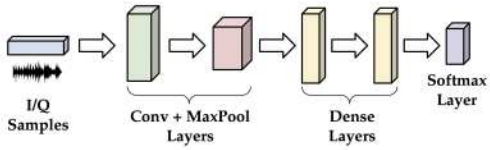

Fig. 5. Architecture of the CNN used for MBC.

After frame synchronization, the data payload is downconverted from its 10-GHz IF and split into baseband I/Q samples. Our DSB 20-GHz signals have a symbol rate of 10 giga-symbols-per-second (GSym/s); thus, our widest baseband BW is 10 GHz. All signals are therefore filtered with a 10-GHz low-pass filter in order to remove image frequencies from the IF downconversion in a BW agnostic manner.

With knowledge of the signal's BW, the signals could be downsampled to one sample per symbol and demodulated at this stage. However, we must assume to not know the signal's BW or symbol rate in order to present valid data to the model. Thus, all waveforms are downsampled by a factor of 8, which keeps them all partially upsampled at a sampling rate of 20 GSa/s. This results in the three different BWs having different levels of upsampling: 8, 4, and 2 for 2.5, 5, and 10 GSym/s, respectively. This partial upsampling also leaves transition samples in our signal, which are apparent in Fig. 4(b). We believe the differing amounts of transition samples is what allows our model to classify the BW of the signal.

With this setup, we transmit signals with different SNR levels, MDs, and BWs. With two SNR levels, five MDs, and three BWs, a total of 30 subsets were collected. Each of these subsets contains 5000 frames, totaling 150 000 frames, with each frame containing 2048 I/Q samples. The dataset is formatted as a concatenation of all samples from all frames. It is sorted in ascending order first by BW, then SNR, and then MD order. Each I/Q sample pair has a corresponding BW, SNR, and MD label. The starting index s of a frame can be calculated as

$$s = (\text{BW} \times 10 + \text{SNR} \times 5 + \text{MD}) \times 5000 \times 2048. \quad (1)$$

The label values are enumerations of their true value, i.e.,

$$\text{BW} \in [0, 1, 2],\ \text{SNR} \in [0, 1],\ \text{MD} \in [0, 1, 2, 3, 4]. \quad (2)$$

B. ML Architecture and Training Procedures

We leverage CNNs to perform MBC, which have been demonstrated to be effective in addressing PHY classification problems such as MD recognition [56] and radio fingerprinting [69]. Their effectiveness is due to the filters in the CVLs, which are able to learn patterns in the I/Q constellation plane regardless of where they occur in the waveform (*shift invariance*) [70]. We consider the CNN architecture shown in Fig. 5. In the article, if not explicitly mentioned otherwise, we refer to this architecture.

We adapted our CNN from the architecture presented in [56], which has shown good results in waveform classification tasks. The input to the network is a tensor of size $(Q, 2)$, where Q is the number of consecutive I/Q samples. In our baseline architecture, the input is processed by seven CVLs, with 64 output filters

of size 1×7. Each of the CVLs is followed by a maximum pooling (MaxPool) layer with filters of size 1×2, which ultimately reduces the output dimension of each CVL in half. Two dense layers follow the CVL + MaxPool layers, each containing 128 neurons. Finally, a Softmax layer to obtain the probability distribution over the set of classes. For the training, validation, and testing phases of learning, the dataset is divided into 65%, 10%, and 25% splits, respectively. The hyperparameters of our baseline architecture are changed to evaluate their performance in Section IV-A, and we show that we can achieve comparable accuracy to the baseline model with shallower networks that use far fewer layers.

Regarding training procedures, CVL layers are trained to learn F filters $\mathbf{P}_f \in \mathbb{R}^{d\times w}, 1 \le f \le F$, where d and w are the depth and width of the filter, respectively. For every $1 \le i \le n'$ and $1 \le j \le m'$, the output of a CVL, defined as $\mathbf{O}^f \in \mathbb{R}^{n'\times m'}$, is computed from the input $\mathbf{I} \in \mathbb{R}^{n\times m}$ as follows:

$$\mathbf{O}^f_{i,j} = \sum_{k=0}^{d-1}\sum_{\ell=0}^{w-1} \mathbf{P}^f_{d-k,w-\ell} \cdot \mathbf{I}_{i-k,j-\ell} \tag{3}$$

where $n' = 1 + \lfloor n + d - 2 \rfloor$ and $m' = 1 + \lfloor m + w - 2 \rfloor$. We use the Adam algorithm [71] as our optimizer with an ℓ_2 regularization parameter $\lambda = 0.0001$, and a learning rate of $l = 0.0001$. We minimize the prediction error through back-propagation, using categorical cross-entropy as a loss function computed on the classifier output. We implement our CNN architecture in Keras running on top of TensorFlow on a system with eight NVIDIA Cuda enabled Tesla V100 GPU.

C. Majority Voting and System Constraints

We leverage a customized boosting procedure [72] based on majority voting [73] to improve the performance of the CNN classifier. The rationale is that, since consecutive PHY frames are likely to belong to the same class, the accuracy of the CNN can be boosted by choosing the class that won the majority among the different runs of the CNN corresponding to the consecutive PHY frames. In addition, our model operates on a max of 2048 I/Q samples, and it is likely that a real data packet will be longer. For our 20-GHz BW signals, this holds 1024 symbols of data, and for 5 GHz, it holds only 256 symbols. Thus, a single data packet could be used to generate multiple CNN inferences, which will ease the constraint of relying on several packets being sent before the channel changes.

More formally, by defining as V the number of consecutive PHY frames, the final class C is selected as follows:

$$C = \arg\max_i \sum_{j=1}^{V} \frac{1}{V} \cdot \hat{p}_{ij} \tag{4}$$

where $\hat{p}_{ij}$ is the probability estimate from the jth classification rule for the ith class.

Fig. 6 shows an example of our algorithm assuming a number of $V = 4$ consecutive PHY frames. Each of these frames is fed to the trained CNN model one at a time as soon as it is received. The output of the CNN corresponding to each frame is coalesced into a single decision by choosing the class that had the majority of votes among the individual CNN outputs.

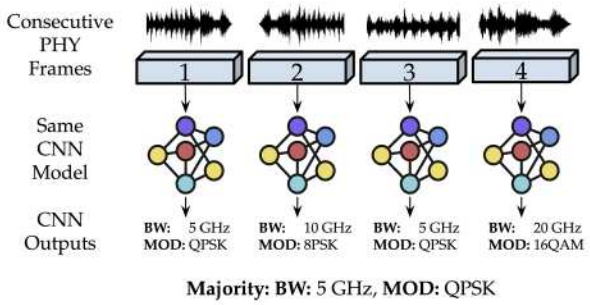

Fig. 6. Majority voting algorithms used to boost accuracy.

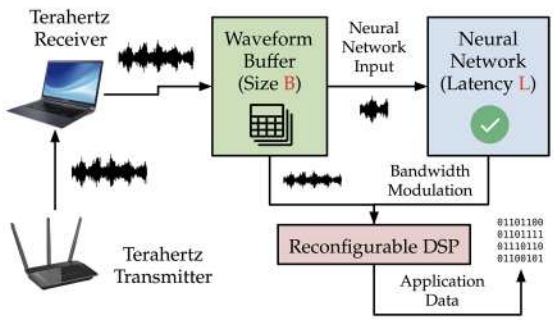

Fig. 7. System constraints in the MBC problem.

A critical constraint that is related to the utilization of a CNN in the DSP loop is that the system has to wait until the CNN computation is completed before the waveform can be demodulated. This implies that the waveform has to be buffered before it can be demodulated. More formally, if the signal has a BW of W MHz, it has to be sampled at $S = 2 \cdot W$ MSa/s according to Nyquist. In our system, each ADC sample is 1 B long. Therefore, S MB need to be buffered each second to avoid overflows. For the sake of generality, we assume the memory available to store waveform samples is B MB, and the latency of the CNN to be L seconds. Fig. 7 visualizes this scenario.

We assume that if the TXer is switching MD and BW parameters every T seconds, the system needs to run the CNN at least once every K times per second to achieve good demodulation performance. Therefore, every T/K seconds, the following operations must be performed:

1) insert $S \cdot (T/K)$ bytes into the waveform buffer;
2) wait for the CNN to complete its execution after L seconds;
3) read the inference results from the CNN;
4) finally reconfigure the DSP and release the buffered waveform.

For simplicity, we will consider (1), (3), and (4) to be negligible with respect to the CNN latency L. As a consequence, the following memory constraint must hold: $B \ge S \cdot \left(\frac{T}{K}\right)$, as well as the following latency constraint must hold: $L \le \frac{T}{K}$. These constraints become extreme due to the significant BW size (i.e., tens of gigahertz) that the RXer has to process.

For example, let us assume that our widest BW of 20 GHz is used. If the TXer switches parameters every $T = 100$ ms, and the RXer runs the CNN $K = 25$ times during each 100-ms period, then the CNN latency $L \leq T/K = 4$ ms (which can be achieved given our results in Section IV-C). The buffer constraint becomes: $B \geq \frac{2 \cdot 20e9 \cdot 100e\text{-}3}{25} = 160$ MB.

Notice that the buffer size B and the sampling rate S usually cannot be relaxed in real-world applications, given they are hard constraints imposed by the platform hardware/RF circuitry. The only parameters that may be modified to meet the requirements are L and K. Although increasing K can help meet the memory constraint, it makes the latency constraint harder to meet. However, if K becomes too small, spectrum data could be stale when the CNN is run (i.e., the TXer has already switched parameters), which can lead to poor performance. Thus, the latency of the CNN, L, has to be decreased in real systems.

IV. Experimental Results

In Section IV-A, we first present the results of a hyperparameter evaluation of our CNN models, as well as the impact of our accuracy boosting technique. Then, in Section IV-B, we present the confusion matrices obtained during the testing phase of the CNNs. Finally, in Section IV-C, we measure the increased computation time with synthesized FPGA latency tests with and without boosting to determine the feasibility of using a CNN on a real-time system.

A. Hyperparameter Evaluation

The hyperparameters of a CNN are the number of CVLs in the network and the amount of output filters in each of those CVLs. We perform hyperparameter evaluation by fully training and testing different networks while incrementing these values to find the optimal architecture. The number of CVLs and output filters affect the number of trainable parameters in the model. Increasing the number of CVLs lowers the amount of trainable parameters (due to max pooling), while increasing the number of output filters raises it. For the models evaluated, the number of trainable parameters ranges from 23 427 (seven CVLs, four filters) to 8 409 103 (one CVL, 128 filters). Fig. 8(a) evaluates the changes for low-SNR input, while Fig. 8(b) evaluates for high-SNR input. The results in Fig. 8 were computed with an input I/Q size of 1024 samples, and the CVLs are followed by two dense layers of 128 nodes each.

From Fig. 8(a) and (b), we find that the best accuracies obtained without boosting are 78% and 90% for low- and high-SNR input data, respectively. This is a considerable result given the amount of classifications and use of experimental data.

We notice that increasing the number of layers and filters per layer increases accuracy up to an extent. As the number of CVL increases past a certain point, the CNN starts to overfit the training dataset, which results in poor accuracy in the test set. For example, the accuracy decreases by 10% when increasing the number of CVLs from five to seven in the low-SNR regime with 128 filters per layer. By the same token, a low amount of filters per layer with a large amount of CVLs results in a low amount of trainable parameters, and performs the poorest.

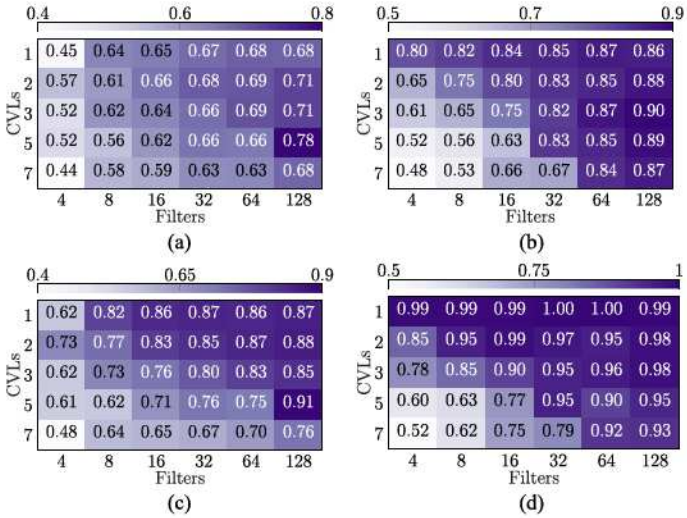

Fig. 8. Hyperparameter evaluation presented with majority voting, $V = 10$, testing accuracy. Plotted as the number of filters per layer versus the number of CVLs. (a) and (b) Standard testing low and high SNR. (c) and (d) Majority voting low and high SNR.

The number of filters per layer is the greatest contributing factor to accuracy. This parameter directly controls the amount of features extracted from the raw waveform data, which in turn controls how much extracted knowledge is passed onto the decision-making dense layers.

To evaluate the effect of our boosting procedure on the performance, Fig. 8(c) and (d) shows the impact of majority voting on the performance of the CNN. The models are tested with $V = 10$ and the results are averaged on 1000 votes for each of the 15 classes. We notice that our boosting technique is able to increase accuracy by up to 21% and 20% in the low- and high-SNR regimes, and achieve top accuracies of 91% and >99%, respectively.

Table II further shows the performance of our boosting technique, as well as evaluating the impact of the input size on the performance. Table II concludes that the amount of I/Q samples fed to the CNN significantly improves the performance of the model. Specifically, the accuracy improves by up to 18% in the low- and high-SNR regime, respectively, when switching from 128 to 2048 I/Q samples and using 64 filters per CVL. We also notice that boosting has a beneficial effect in both SNR regimes, which helps improve performance by close to 10% in the high-SNR regime.

Table II also shows the performance of our majority voting boosting algorithm as a function of the number of consecutive frames per vote V. Specifically it compares the performance when testing with two, five, seven, and ten consecutive frames per vote. The results show that the boosting performance increases with V, yet it reaches a plateau when $V = 10$.

B. Confusion Matrices

Fig. 9 reports our specific classification results with confusion matrix plots for three CNN architectures trained on our two

TABLE II
COMPARISON OF INCREASING V VOTES IN EACH MAJORITY VOTING, AND EFFECTS OF MAJORITY VOTING ON MODEL WITH INCREASING INPUT SIZES

SNR	K	Input	Standard testing	Majority votes V: 2	5	7	10
Low	16	128	42.90%	43.5%	49.6%	50.5%	51.1%
Low	16	1024	58.90%	59.2%	63.9%	64.9%	65.4%
Low	16	2048	66.40%	65.5%	72.6%	73.9%	74.8%
Low	64	128	52.70%	53.6%	57.2%	57.6%	57.8%
Low	64	1024	63.20%	65.1%	68.7%	69.0%	69.7%
Low	64	2048	70.20%	71.7%	75.7%	76.4%	76.4%
Average Increase Above Standard				**0.7%**	**5.6%**	**6.3%**	**6.8%**
Average Increase Above Previous V					**4.9%**	**0.8%**	**0.5%**
High	16	128	47.00%	46.3%	51.7%	52.9%	54.5%
High	16	1024	66.20%	66.0%	74.2%	75.3%	75.0%
High	16	2048	63.40%	62.8%	71.7%	72.8%	73.4%
High	64	128	71.60%	68.9%	82.2%	85.4%	87.2%
High	64	1024	83.90%	86.3%	89.1%	90.2%	92.0%
High	64	2048	90.10%	91.3%	95.3%	95.7%	96.3%
Average Increase Above Standard				**-0.1%**	**7.0%**	**8.4%**	**9.4%**
Average Increase Above Previous V					**7.1%**	**1.4%**	**1.0%**

Notes: All models used seven CVLs. K is the amount of output filters per CVL.

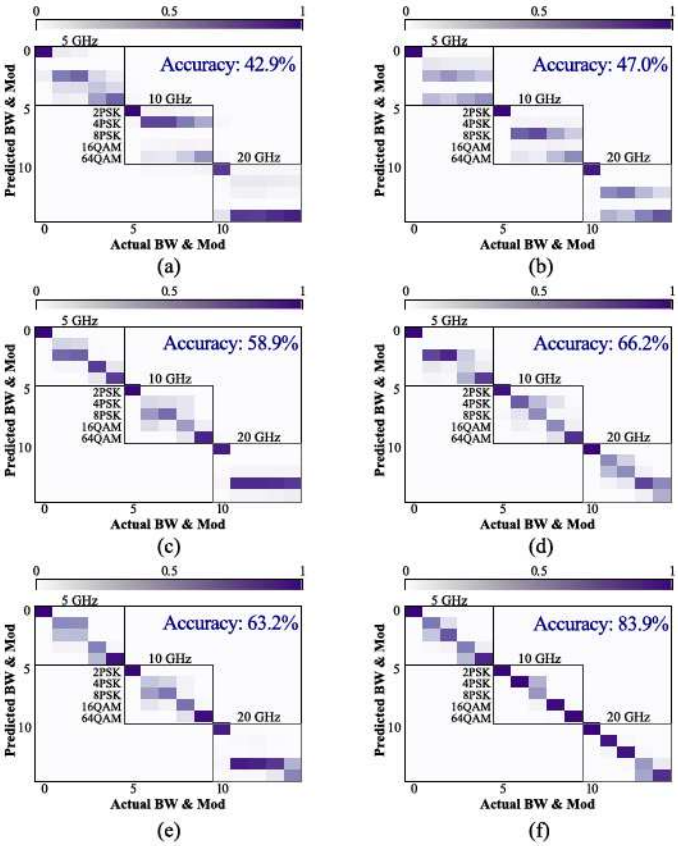

Fig. 9. (a), (c), and (e) Confusion matrices for low-SNR and (b), (d), and (f) high-SNR testing accuracies without boosting. All models use seven CVLs followed by two dense layers with 128 nodes each, but use different numbers of filters in each CVL and numbers of samples in the input data. (a) and (b) 16 filters, 128 samples. (c) and (d) 16 filters, 1024 samples. (e) and (f) 64 filters, 1024 samples.

TABLE III
STANDARD TESTING AND MAJORITY VOTING ($V = 10$) ACCURACIES FOR SIX MODELS AND THEIR CORRESPONDING COMPUTATION TIMES ON SYNTHESIZED FPGA CIRCUITS

CVLs	Filters	Testing accuracy: Low SNR	High SNR	Both SNR	FPGA latency
Standard testing					
1	32	67%	85%	67%	4ms
1	64	68%	87%	67%	9ms
1	128	68%	86%	67%	95ms
3	32	66%	82%	73%	78ms
3	64	69%	87%	79%	303ms
3	128	71%	90%	81%	1180ms
Majority voting, V = 10					
1	32	87%	99%	86%	43ms
1	64	86%	99%	88%	93ms
1	128	87%	99%	86%	952ms
3	32	80%	95%	88%	780ms
3	64	83%	96%	91%	3030ms
3	128	85%	98%	92%	11 800ms

SNR levels. Our results conclude that all the models are able to perfectly classify the BW of the signal in both SNR regimes.

We notice that a model trained with less filters is still able to achieve reliable classification of 2PSK, whereas higher order MDs become indistinguishable, especially in the low-SNR scenario. However, we find that increasing the number of filters in the CVLs severely impacts the accuracy of the model, achieving 83.9% in the case of 64 filters and 1024 I/Q input size, as shown in Fig. 9(f).

C. FPGA-Based CNN Latency Analysis

To have an estimation of the CNN latency involved in a real system, we have synthesized some of the CNNs trained in Section IV-A into FPGA-compliant circuits. Table III shows the standard and boosted accuracies for select models with different numbers of CVLs and filters and the added latency when run on an FPGA. In all these experiments, we have leveraged high-level synthesis (HLS) to translate the C++-level description of the CNN directly into hardware-based Verilog language. HLS is by no means the most efficient synthesis process, and improved latency results can be reached with different strategies.

The circuits were synthesized assuming a clock period of 5 ns (clock speed of 200 MHz). The target FPGA is a XC7Z045FFG900-2 from Xilinx, an FPGA commonly used in SDR devices. The latency estimations are based upon a pipelined FPGA design presented in [51].

Table III presents majority voting accuracies using $V = 10$ compared to standard testing accuracies. The smallest model tested (one CVL, 32 filters) is able to achieve 99% boosted accuracy with the high-SNR regime and outperform the largest model's (three CVL, 128 filters) standard testing accuracy by 9% while executing more than 20 times faster. We notice that increasing the number of CVLs and filters exponentially increases the latency. This result validates the efficacy of majority voting and drives the effort to design small, shallow networks.

V. Conclusion

The THz band is one of the last resorts to withstand the staggering growth in mobile connectivity experienced over the last few years, and that is expected to continue in the future. The severely dynamic channel BW in the THz band implies that techniques able to demodulate BW-dynamic transmissions will become mandatory in the years to come. The experiments presented in this article have proven for the first time that relatively small neural networks, including single-layer CNNs, can be successfully used to address the MBC problem at THz frequencies, which paves the way to their usage in actual THz systems. Our FPGA analysis has shown that small models can achieve high accuracies with boosting and still maintain low latency, though it may not be enough for extremely fast-changing channels.

Future research efforts will be devoted to further reducing FPGA latency through smaller neural networks and better optimization to enable use in real-time systems. Expanding the model to classify smaller increments in BW would greatly increase its capabilities. However, this tougher challenge would call for changing architecture to a hierarchical model where BW and MD are different classifiers. We will also leverage transfer learning to train our models on data affected by absorption windows when THz and ultra-broadband technology matures. We hope that our findings will drive existing standardization efforts in the THz bands, which may consider the usage of data-driven techniques to implement BW-dynamic systems.

Acknowledgment

The views expressed are those of the authors and do not reflect the official guidance or position of the United States Government, the Department of Defense or of the United States Air Force. The experimental dataset was collected by Northeastern University team and will be disseminated per DoD memorandum on Fundamental Research dated 24 May 2010. Approved for public release. AFRL-2023-0140.

References

[1] Ericsson Incorporated, "Ericsson mobility report," 2020. [Online]. Available: https://tinyurl.com/EricssonMob2020

[2] M. Shafi et al., "5G: A tutorial overview of standards, trials, challenges, deployment, and practice," *IEEE J. Sel. Areas Commun.*, vol. 35, no. 6, pp. 1201–1221, Jun. 2017.

[3] I. F. Akyildiz, J. M. Jornet, and C. Han, "TeraNets: Ultra-broadband communication networks in the terahertz band," *IEEE Wireless Commun.*, vol. 21, no. 4, pp. 130–135, Aug. 2014.

[4] T. S. Rappaport et al., "Wireless communications and applications above 100 GHz: Opportunities and challenges for 6G and beyond," *IEEE Access*, vol. 7, pp. 78729–78757, 2019.

[5] M. Giordani, M. Polese, M. Mezzavilla, S. Rangan, and M. Zorzi, "Toward 6G networks: Use cases and technologies," *IEEE Commun. Mag.*, vol. 58, no. 3, pp. 55–61, Mar. 2020.

[6] M. Polese, J. M. Jornet, T. Melodia, and M. Zorzi, "Toward end-to-end, full-stack 6G terahertz networks," *IEEE Commun. Mag.*, vol. 58, no. 11, pp. 48–54, Nov. 2020.

[7] J. M. Jornet and I. F. Akyildiz, "Channel modeling and capacity analysis for electromagnetic wireless nanonetworks in the terahertz band," *IEEE Trans. Wireless Commun.*, vol. 10, no. 10, pp. 3211–3221, Oct. 2011.

[8] A. Cohen et al., "Absolute security in high-frequency wireless links," *IEEE J. Sel. Topics Signal process.*, submitted for publication.

[9] Z. Fang, H. Guerboukha, R. Shrestha, M. Hornbuckle, Y. Amarasinghe, and D. M. Mittleman, "Secure communication channels using atmosphere-limited line-of-sight terahertz links," *IEEE Trans. THz Sci. Technol.*, vol. 12, no. 4, pp. 363–369, Apr. 2022.

[10] R. Shrestha, H. Guerboukha, Z. Fang, E. Knightly, and D. Mittleman, "Jamming a terahertz wireless link," *Nature Commun.*, vol. 13, 2022, Art. no. 3045.

[11] S. Venkatesh, X. lu, B. Tang, and K. Sengupta, "Secure space–time-modulated millimetre-wave wireless links that are resilient to distributed eavesdropper attacks," *Nature Electron.*, vol. 4, pp. 827–836, 2021.

[12] J. Ma et al., "Security and eavesdropping in terahertz wireless links," *Nature*, vol. 563, no. 7729, pp. 89–93, Nov. 2018.

[13] T. D. Vo-Huu, T. D. Vo-Huu, and G. Noubir, "Interleaving jamming in Wi-Fi networks," in *Proc. ACM Conf. Secur. Privacy Wireless Mobile Netw.*, 2016, pp. 31–42.

[14] T. C. Clancy, "Efficient OFDM denial: Pilot jamming and pilot nulling," in *Proc. IEEE Int. Conf. Commun.*, 2011, pp. 1–5.

[15] M. L. D. Wong and A. K. Nandi, "Automatic digital modulation recognition using spectral and statistical features with multi-layer perceptrons," in *Proc. IEEE 6th Int. Symp. Signal Process. Appl.*, 2001, pp. 390–393.

[16] J. L. Xu, W. Su, and M. Zhou, "Software-defined radio equipped with rapid modulation recognition," *IEEE Trans. Veh. Technol.*, vol. 59, no. 4, pp. 1659–1667, May 2010.

[17] S. U. Pawar and J. F. Doherty, "Modulation recognition in continuous phase modulation using approximate entropy," *IEEE Trans. Inf. Forensics Secur.*, vol. 6, no. 3, pp. 843–852, Sep. 2011.

[18] Q. Shi and Y. Karasawa, "Automatic modulation identification based on the probability density function of signal phase," *IEEE Trans. Commun.*, vol. 60, no. 4, pp. 1033–1044, Apr. 2012.

[19] S. Ghodeswar and P. G. Poonacha, "An SNR estimation based adaptive hierarchical modulation classification method to recognize M-ary QAM and M-ary PSK signals," in *Proc. IEEE 3rd Int. Conf. Signal Process. Commun. Netw.*, 2015, pp. 1–6.

[20] *IEEE Standard for High Data Rate Wireless Multi-Media Networks–Amendment 2: 100 Gb/s Wireless Switched Point-to-Point Physical Layer*, IEEE Standard 802.15.3d-2017, 2017.

[21] Institute of Electrical and Electronic Engineers (IEEE), "IEEE 802.15 WPAN Terahertz Interest Group (IGthz)," 2021. [Online]. Available: https://www.ieee802.org/15/pub/IGthzOLD.html

[22] H. Sarieddeen, N. Saeed, T. Y. Al-Naffouri, and M.-S. Alouini, "Next generation terahertz communications: A rendezvous of sensing, imaging, and localization," *IEEE Commun. Mag.*, vol. 58, no. 5, pp. 69–75, May 2020.

[23] J. Ma, F. Vorrius, L. Lamb, L. Moeller, and J. F. Federici, "Experimental comparison of terahertz and infrared signaling in laboratory-controlled rain," *J. Infrared MillimeterTHz Waves*, vol. 36, no. 9, pp. 856–865, 2015.

[24] L. S. Rothman et al., "The HITRAN 2008 molecular spectroscopic database," *J. Quantitative Spectrosc. Radiative Transf.*, vol. 110, no. 9/10, pp. 533–572, 2009.

[25] R. M. Goody and Y. L. Yung, *Atmospheric Radiation: Theoretical Basis*. London, U.K.: Oxford Univ. Press, 1995.

[26] C. Han, A. O. Bicen, and I. F. Akyildiz, "Multi-wideband waveform design for distance-adaptive wireless communications in the terahertz band," *IEEE Trans. Signal Process.*, vol. 64, no. 4, pp. 910–922, Feb. 2015.

[27] J. M. Jornet and I. F. Akyildiz, "Femtosecond-long pulse-based modulation for terahertz band communication in nanonetworks," *IEEE Trans. Commun.*, vol. 62, no. 5, pp. 1742–1754, May 2014.

[28] Z. Hossain and J. M. Jornet, "Hierarchical bandwidth modulation for ultra-broadband terahertz communications," in *Proc. IEEE Int. Conf. Commun.*, 2019, pp. 1–7.

[29] Y. Yu, T. Wang, and S. C. Liew, "Deep-reinforcement learning multiple access for heterogeneous wireless networks," *IEEE J. Sel. Areas Commun.*, vol. 37, no. 6, pp. 1277–1290, Jun. 2019.

[30] S. Wang, H. Liu, P. H. Gomes, and B. Krishnamachari, "Deep reinforcement learning for dynamic multichannel access in wireless networks," *IEEE Trans. Cogn. Commun. Netw.*, vol. 4, no. 2, pp. 257–265, Feb. 2018.

[31] O. Naparstek and K. Cohen, "Deep multi-user reinforcement learning for distributed dynamic spectrum access," *IEEE Trans. Wireless Commun.*, vol. 18, no. 1, pp. 310–323, Jan. 2019.

[32] H.-H. Chang et al., "Distributive dynamic spectrum access through deep reinforcement learning: A reservoir computing based approach," *IEEE Internet Things J.*, vol. 6, no. 2, pp. 1938–1948, Apr. 2019.

[33] H. Pang, C. Zhang, F. Wang, J. Liu, and L. Sun, "Towards low latency multi-viewpoint 360° interactive video: A multimodal deep reinforcement learning approach," in *Proc. IEEE Conf. Comput. Commun.*, 2019, pp. 991–999.

[34] F. Wang et al., "Intelligent edge-assisted crowdcast with deep reinforcement learning for personalized QoE," in *Proc. IEEE Conf. Comput. Commun.*, 2019, pp. 910–918.
[35] Y. Zhang et al., "DRL360: 360-degree video streaming with deep reinforcement learning," in *Proc. IEEE Conf. Comput. Commun.*, 2019, pp. 1252–1260.
[36] J. Liu, B. Krishnamachari, S. Zhou, and Z. Niu, "DeepNap: Data-driven base station sleeping operations through deep reinforcement learning," *IEEE Internet Things J.*, vol. 5, no. 6, pp. 4273–4282, Dec. 2018.
[37] Z. Wang, L. Li, Y. Xu, H. Tian, and S. Cui, "Handover control in wireless systems via asynchronous multiuser deep reinforcement learning," *IEEE Internet Things J.*, vol. 5, no. 6, pp. 4296–4307, Jun. 2018.
[38] L. Zhang, J. Tan, Y. Liang, G. Feng, and D. Niyato, "Deep reinforcement learning based modulation and coding scheme selection in cognitive heterogeneous networks," *IEEE Trans. Wireless Commun.*, vol. 18, no. 6, pp. 3281–3294, Jun. 2019.
[39] M. Feng and S. Mao, "Dealing with limited backhaul capacity in millimeter-wave systems: A deep reinforcement learning approach," *IEEE Commun. Mag.*, vol. 57, no. 3, pp. 50–55, Mar. 2019.
[40] Y. He, N. Zhao, and H. Yin, "Integrated networking, caching, and computing for connected vehicles: A deep reinforcement learning approach," *IEEE Trans. Veh. Technol.*, vol. 67, no. 1, pp. 44–55, Jan. 2018.
[41] Y. Sun, M. Peng, and S. Mao, "Deep reinforcement learning-based mode selection and resource management for green fog radio access networks," *IEEE Internet Things J.*, vol. 6, no. 2, pp. 1960–1971, Apr. 2019.
[42] R. Li et al., "Deep reinforcement learning for resource management in network slicing," *IEEE Access*, vol. 6, pp. 74429–74441, 2018.
[43] H. Zhang, W. Li, S. Gao, X. Wang, and B. Ye, "ReLeS: A neural adaptive multipath scheduler based on deep reinforcement learning," in *Proc. IEEE Conf. Comput. Commun.*, 2019, pp. 1648–165.
[44] Q. Mao, F. Hu, and Q. Hao, "Deep learning for intelligent wireless networks: A comprehensive survey," *IEEE Commun. Surv. Tut.*, vol. 20, no. 4, pp. 2595–2621, Apr. 2018.
[45] Y. Wang, M. Liu, J. Yang, and G. Gui, "Data-driven deep learning for automatic modulation recognition in cognitive radios," *IEEE Trans. Veh. Technol.*, vol. 68, no. 4, pp. 4074–4077, Apr. 2019.
[46] N. E. West and T. O' Shea, "Deep architectures for modulation recognition," in *Proc. IEEE Int. Symp. Dyn. Spectr. Access Netw.*, 2017, pp. 1–6.
[47] K. Karra, S. Kuzdeba, and J. Petersen, "Modulation recognition using hierarchical deep neural networks," in *Proc. IEEE Int. Symp. Dyn. Spectr. Access Netw.*, 2017, pp. 1–3.
[48] S. Peng et al., "Modulation classification based on signal constellation diagrams and deep learning," *IEEE Trans. Neural Netw. Learn. Syst.*, vol. 30, no. 3, pp. 718–727, Mar. 2018.
[49] F. Meng, P. Chen, L. Wu, and X. Wang, "Automatic modulation classification: A deep learning enabled approach," *IEEE Trans. Veh. Technol.*, vol. 67, no. 11, pp. 10760–10772, Nov. 2018.
[50] F. Restuccia and T. Melodia, "Big data goes small: Real-time spectrum-driven embedded wireless networking through deep learning in the RF loop," in *Proc. IEEE Conf. Comput. Commun.*, 2019, pp. 2152–2160.
[51] F. Restuccia and T. Melodia, *PolymoRF: Polymorphic Wireless Receivers Through Physical-Layer Deep Learning*. New York, NY, USA: ACM, 2020, pp. 271–280.
[52] E. Like, V. Chakravarthy, R. Husnay, and Z. Wu, "Modulation recognition in multipath fading channels using cyclic spectral analysis," in *Proc. IEEE Glob. Telecommun. Conf.*, 2008, pp. 1–6.
[53] Y. Zhang, D. Liu, J. Liu, Y. Xian, and X. Wang, "Improved deep neural network for OFDM signal recognition using hybrid grey wolf optimization," *IEEE Access*, vol. 8, pp. 133622–133632, 2020.
[54] V. A. Pavlov, S. V. Zavjalov, S. V. Volvenko, and A. Gorlov, "Deep learning application for classification of SEFDM signals," in *Proc. IEEE Int. Conf. Elect. Eng. Photon.*, 2021, pp. 28–31.
[55] A. Al-Shawabka et al., "Exposing the fingerprint: Dissecting the impact of the wireless channel on radio fingerprinting," in *Proc. IEEE Conf. Comput. Commun.*, 2020, pp. 646–655.
[56] T. J. O'Shea, T. Roy, and T. C. Clancy, "Over-the-air deep learning based radio signal classification," *IEEE J. Sel. Topics Signal Process.*, vol. 12, no. 1, pp. 168–179, Feb. 2018.
[57] K. Karra, S. Kuzdeba, and J. Petersen, "Modulation recognition using hierarchical deep neural networks," in *Proc. IEEE Int. Symp. Dyn. Spectr. Access Netw.*2017, pp. 1–3.
[58] M. Kulin, T. Kazaz, I. Moerman, and E. D. Poorter, "End-to-end learning from spectrum data: A deep learning approach for wireless signal identification in spectrum monitoring applications," *IEEE Access*, vol. 6, pp. 18484–18501, 2018.
[59] M. Polese, F. Restuccia, and T. Melodia, "DeepBeam: Deep Waveform learning for coordination-free beam management in mmWave networks," in *Proc. 22nd Int. Symp. Theory, Algo. Found. Protocol Des. Mobile Netw. Mobile Comput.*, 2021, pp. 61–70.
[60] Y. Zhang, M. Alrabeiah, and A. Alkhateeb, "Learning beam codebooks with neural networks: Towards environment-aware mmWave MIMO," in *Proc. IEEE 21st Int. Workshop Signal Process. Adv. Wireless Commun.*, 2020, pp. 1–5.
[61] M. Alrabeiah and A. Alkhateeb, "Deep learning for mmWave beam and blockage prediction using sub-6 GHz channels," *IEEE Trans. Commun.*, vol. 68, no. 9, pp. 5504–5518, Sep. 2020.
[62] Y. Jin, J. Zhang, B. Ai, and X. Zhang, "Channel estimation for mmWave massive MIMO with convolutional blind denoising network," *IEEE Commun. Lett.*, vol. 24, no. 1, pp. 95–98, Jan. 2019.
[63] S. Fan, Y. Wu, C. Han, and X. Wang, "A structured bidirectional LSTM deep learning method for 3D terahertz indoor localization," in *Proc. IEEE Conf. Comput. Commun.*, 2020, pp. 2381–2390.
[64] S. Fan, Y. Wu, C. Han, and X. Wang, "SIABR: A. structured intra-attention bidirectional recurrent deep learning method for ultra-accurate terahertz indoor localization," *IEEE J. Sel. Areas Commun.*, vol. 39, no. 7, pp. 2226–2240, Jul. 2021.
[65] Y. Chen and C. Han, "Deep CNN-based spherical-wave channel estimation for terahertz ultra-massive MIMO systems," in *Proc. IEEE Glob. Commun. Conf.*, 2020, pp. 1–6.
[66] J. Federici and L. Moeller, "Review of terahertz and subterahertz wireless communications," *J. Appl. Phys.*, vol. 107, no. 11, 2010, Art. no. 111101.
[67] P. Sen et al., "The TeraNova platform: An integrated testbed for ultra-broadband wireless communications at true terahertz frequencies," *Comput. Netw.*, vol. 179, 2020, Art. no. 107370.
[68] H. Ganapathy, D. A. Pados, and G. N. Karystinos, "New bounds and optimal binary signature sets—Part II: Aperiodic total squared correlation," *IEEE Trans. Commun.*, vol. 59, no. 5, pp. 1411–1420, May 2011.
[69] F. Restuccia et al., "DeepRadioID: Real-time channel-resilient optimization of deep learning-based radio fingerprinting algorithms," in *Proc. 20th ACM Int. Symp. Mobile Ad Hoc Netw. Comput.*, 2019, pp. 51–60.
[70] F. Restuccia and T. Melodia, "Deep learning at the physical layer: System challenges and applications to 5G and beyond," *IEEE Commun. Mag.*, vol. 58, no. 10, pp. 58–64, Oct. 2020.
[71] D. P. Kingma and J. Ba, "Adam: A method for stochastic optimization," in *Proc. 3rd Int. Conf. Learn. Representations*, 2015.
[72] R. E. Schapire, "The boosting approach to machine learning: An overview," *Nonlinear Estimation Classification*, Berlin, Germany: Springer, 2003, pp. 149–171.
[73] D. Ruta and B. Gabrys, "Classifier selection for majority voting," *Inf. Fusion*, vol. 6, no. 1, pp. 63–81, 2005.

Jacob Hall (Member, IEEE) received the B.S. degree in electrical and computer engineering from the State University of New York Polytechnic Institute, Utica, NY, USA, in 2020, and the M.S. degree in electrical and computer engineering from Northeastern University, Boston, MA, USA, in 2022.

His M.S. degree was funded by the DoD's SMART Scholarship-for-Service Program with the Air Force Research Laboratory (AFRL) Information Directorate, Rome, NY, USA, as his sponsor. He is currently with AFRL under their THz program. His research interests include deep learning and THz communications.

Josep Miquel Jornet (Senior Member, IEEE) received the Engineering degree in telecommunication engineering and the Master of Science degree in information and communication technologies from the Universitat Politècnica de Catalunya, Barcelona, Spain, in 2008, and the Ph.D. degree in electrical and computer engineering from the Georgia Institute of Technology, Atlanta, GA, USA, in August 2013.

He is currently an Associate Professor with the Department of Electrical and Computer Engineering, the Director of the Ultrabroadband Nanonetworking (UN) Laboratory, and a Member of the Institute for the Wireless Internet of Things and the SMART Center, Northeastern University, Boston, MA, USA. He has coauthored more than 220 peer-reviewed scientific publications, including one book and five U.S. patents in the areas of his research interests, which include terahertz communications, wireless nano-bio-communication networks, and the Internet of Nano-Things.

Dr. Jornet is the Lead PI on multiple grants from U.S. federal agencies including the National Science Foundation, Air Force Office of Scientific Research, and Air Force Research Laboratory, as well as industry. He was the recipient of multiple awards, including the 2017 IEEE ComSoc Young Professional Best Innovation Award, the 2017 ACM NanoCom Outstanding Milestone Award, the NSF CAREER Award in 2019, the 2022 IEEE ComSoc RCC Early Achievement Award, and the 2022 IEEE Wireless Communications Technical Committee Outstanding Young Researcher Award, among others, as well as four best paper awards. He is an IEEE ComSoc Distinguished Lecturer (Class of 2022-2023). He is also the Editor-in-Chief of the Elsevier *Nano Communication Networks* journal and an Editor for IEEE TRANSACTIONS ON COMMUNICATIONS.

Ngwe Thawdar (Member, IEEE) received the B.Sc. degree from the Binghamton University, Binghamton, NY, USA, in 2009, and the M.Sc. and Ph.D. degrees from the State University of New York University at Buffalo, Buffalo, NY, in 2011 and 2018, respectively, all in electrical engineering.

Since 2012, she has been with Air Force Research Laboratory Information Directorate, Rome, NY. Her research includes wireless spread spectrum communications, cooperative communications, and software-defined radio implementation. Her current research focuses on communications and networking in emerging spectral bands such as mm-waves and terahertz band frequencies.

Dr. Thawdar was the recipient of the 2019 AFRL Early Career Award, the 2021 AFRL Information Directorate Scientist/Engineer of the Year award, and the 2022 IEEE International Conference on Communications Best Paper Award.

Tommaso Melodia (Fellow, IEEE) received the Laurea (integrated B.S. and M.S.) degree in telecommunications engineering from the University of Rome–La Sapienza, Rome, Italy, in 2001, and the Ph.D. degree in electrical and computer engineering from the Georgia Institute of Technology, Atlanta, GA, USA, in 2007.

He is currently the William Lincoln Smith Professor with the Department of Electrical and Computer Engineering, Northeastern University, Boston, MA, USA. He is also the Founding Director of the Institute for the Wireless Internet of Things and the Director of Research for the PAWR Project Office. He is the author or coauthor of more than 250 papers published in international journals, books, and conferences.

Dr. Melodia was the recipient of the National Science Foundation CAREER Award. He is the Editor-in-Chief of *Computer Networks*. He is a co-founder of 6G Symposium, and was the Technical Program Committee Chair for IEEE Infocom 2018, and the General Chair for ACM MobiHoc 2020, IEEE SECON 2019. His research is funded by U.S. industry and a number of Federal agencies including the U.S. National Science Foundation, the Office of the Undersecretary of Defense, Air Force Research Laboratory, the Office of Naval Research, DARPA, the Army Research Laboratory, the Department of Transportation, IARPA, and NASA. He is an Associate Editor-in-Chief of IEEE COMMUNICATIONS SURVEYS AND TUTORIALS, and a Senior Editor of IEEE TRANSACTIONS ON GREEN COMMUNICATIONS AND NETWORKING.

Francesco Restuccia (Senior Member, IEEE) received the B.S. and M.S. degrees in computer engineering with highest honors from the University of Pisa, Pisa, Italy, in 2009 and 2011, respectively, and the Ph.D. degree in computer science from the Missouri University of Science and Technology, Rolla, MO, USA, in 2016.

He is currently an Assistant Professor with the Department of Electrical and Computer Engineering, and a Member of the Institute for the Wireless Internet of Things and the Roux Institute, Northeastern University, Boston, MA, USA. He has authored or coauthored more than 60 papers in top-tier venues in computer networking, as well as coauthored 16 U.S. patents and three book chapters. His research focuses on the design and experimental evaluation of next-generation edge-assisted data-driven wireless systems.

Dr. Restuccia's research is funded by several grants from the U.S. National Science Foundation and the Department of Defense. He was the recipient of the Office of Naval Research Young Investigator Award, the Air Force Office of Scientific Research Young Investigator Award, and the Mario Gerla Award in Computer Science, as well as Best Paper Awards at IEEE INFOCOM and IEEE WOWMOM. He regularly serves as a TPC Member and Reviewer for several ACM and IEEE conferences and journals.